ACCEPTED MANUSCRIPT

Embedding of human vertebral bodies leads to higher ultimate load and altered damage localisation under axial compression

G.Maquer, J.J.Schwiedrzik and P.K.Zysset*

Ghislain Maquer
Institute of Surgical Technology and Biomechanics, University of Bern, Bern, Switzerland
Stauffacherstr. 78
CH-3014 Bern
Tel +41 (0)31 631 5928
Fax. +41 (0)31 631 5960
ghislain.maquer@istb.unibe.ch

Johann Jakob Schwiedrzik
Institute of Surgical Technology and Biomechanics, University of Bern, Bern, Switzerland
Stauffacherstr. 78
CH-3014 Bern
Tel. +41 (0)31 631 5928
Fax. +41 (0)31 631 5960
jakob.schwiedrzik@istb.unibe.ch

Philippe Kurt Zysset (Corresponding author)
Institute of Surgical Technology and Biomechanics, University of Bern, Bern, Switzerland
Stauffacherstr. 78
CH-3014 Bern
Tel: +41 31 631 59 25
Fax: +41 31 631 59 60
philippe.zysset@istb.unibe.ch

*Corresponding author. Email: philippe.zysset@istb.unibe.ch

Embedding of human vertebral bodies leads to higher ultimate load and altered damage localisation under axial compression

Computer tomography (CT-) based finite element (FE) models of vertebral bodies assess fracture load *in vitro* better than DXA, but boundary conditions affect stress distribution under the endplates that may influence ultimate load and damage localization under post-yield strains. Therefore, HRpQCT-based homogenized FE models of 12 vertebral bodies were subjected to axial compression with two distinct boundary conditions: embedding in polymethylmethalcrylate (PMMA) and bonding to a healthy intervertebral disc (IVD) with distinct hyperelastic properties for nucleus and annulus. Bone volume fraction and fabric assessed from HRpQCT data were used to determine the elastic, plastic and damage behaviour of bone. Ultimate forces obtained with PMMA were 22% higher than with IVD but correlated highly (R^2=0.99). At ultimate force, distinct fractions of damage were computed in the endplates (PMMA: 6%, IVD: 70%), cortex and trabecular sub-regions, which confirms previous observations that in contrast to PMMA embedding, failure initiated underneath the nuclei in healthy IVDs. In conclusion, axial loading of vertebral bodies via PMMA embedding versus healthy IVD overestimates ultimate load and leads to distinct damage localization and failure pattern.

Keywords: boundary conditions; finite element analysis; osteoporosis; vertebral strength; intervertebral disc

1. Introduction

With 490 000 cases a year in Europe, compression fractures of osteoporotic vertebrae are among the most common type of osteoporotic fractures with high morbidity and health care costs (Johnell and Kanis 2005). Dual energy X-ray absorptiometry (DXA), the usual technique for diagnosis and follow up of osteoporosis in the vertebra, does not account for morphology and local variation of bone density and thus, is not a satisfactory surrogate of bone strength (Griffith and Genant 2008, McDonnell et al. 2007, Dall'Ara et al. 2012). Yet, more advanced methods such as QCT, HRQCT and CT-based finite element (FE) models are now used in clinical trials to estimate vertebral bone strength for various load cases (Keaveny et al. 2007, Graeff et al. 2009).

Several studies suggest that vertebral strength is more sensitive to the boundary condition on the endplates than to bone quality (Buckley et al. 2006, Jones and Wilcox 2007). Therefore, due to the uncertainties introduced by various degrees of disc degeneration in elderly spines, validation of the FE models were performed with endplates embedded in PMMA (Crawford et al. 2003, Chevalier et al. 2009) or without endplates (Dall'ara et al. 2010). These boundary conditions, recently found to be equivalent (Maquer et al. 2012), may be appropriate for mimicking a highly degenerated IVD that applies a more uniform load on the endplates compared to a healthy IVD (Keller et al. 1993).

However, a higher proportion of wedge fractures is observed clinically for vertebral bodies adjacent to degenerated IVD, while patients with healthy IVD rather undergo biconcave fractures (Seymour et al. 1998, Lee 2000, Ortiz et al. 2011). Thus, the absence of endplates or their embedding would probably generate boundary conditions that are different from a healthy IVD and may lead to distinct structural properties.

In fact, several authors simulated intervertebral discs as boundary condition for their µFE models of vertebral bodies but only stress or strain distributions were computed and linear elastic models of the IVD were used (Homminga et al. 2004, Eswaran et al. 2006, Eswaran et al. 2007, Fields et al. 2010). The recent introduction of hyper-elastic and anisotropic models of intervertebral disc would guarantee a more realistic boundary condition but such models were only used to investigate disc degeneration (Galbusera et al. 2011) and its effects on the range of motion and stiffness of the spine (Rohlmann et al. 2006) or on the disc stress profile (Dolan et al. 2001).

Thus, while damage and strength of embedded vertebral bodies have been computed in some FE studies, the literature is poor in case of specimens surrounded by intervertebral discs. Furthermore, although boundary conditions are a critical aspect of biomechanical testing, its impact on the failure behaviour of the vertebral body remains unclear as no comparison between PMMA embedding and

intervertebral discs was undertaken.

Accordingly, the aim of this work was to determine whether strength and damage localisation predictions computed from homogenized finite elements models of human vertebral bodies were influenced by the choice of boundary condition. To this end, two sets of models based on 12 samples were produced before axial compression was applied: either embedding in PMMA was simulated as often done in biomechanical studies *in vitro* or the specimens were surrounded by healthy intervertebral discs.

2. Materials and Methods

An overview of the automatic homogenized finite element (hFE) model generation is given in Figure1.

2.1. CT scans of the vertebral bodies

HRpQCT data of 12 vertebral bodies taken from another study (Chevalier et al. 2008) were used to generate the FE models (Figure 1). The authors extracted the vertebrae (L1-L5, age 47-83, all male), removed the soft tissues, sectioned the posterior elements at the pedicles and scanned the vertebral bodies in a water-filled container (XtremeCT, 82 μm, 59.4 kV, 1000 mA, Scanco Medical AG, Zürich, Switzerland).

2.2. Image processing

The image processing and meshing were performed automatically with in-house software onthe HRpQCT data following a published method (Pahr and Zysset 2008). A Laplace–Hamming filter was first used to remove noise (Laib et al. 1998), the images were then scaled to a range of 1–250 and segmented between cortical and trabecular masks using a ‘fill’ algorithm described by Pahr and Zysset (2008) (Figure 1).

2.3. Mesh generation

Isosurf (Treece et al. 1999) was used to create a triangle mesh on the surface of the trabecular mask. This was only a surface mesh without cortex representation yet. Therefore, to produce volume meshes for trabecular and cortical bone, the algorithm described in Pahr and Zysset 2008 was used. This algorithm generates quadratic wedge elements for the cortex by extruding the positions of the

nodes of the triangle mesh until the thickness of the wedge elements and the local thickness of the cortical mask matches. The trabecular bone was meshed by generating quadratic tetrahedral elements within the volume determined by the triangle mesh. Endplate elements were selected from the cortex elementset based on the angle between the normal of the triangular surface and the anatomical cranio-caudal direction. Compared to the published procedure, an extra step became necessary. The meshes were imported in Cubit (Cubit mesh generation environment, Version 12.2, CUBIT Development Team, Sandia National Laboratory, Albuquerque) and the endplate elements were remeshed in order to account for the morphology of the nucleus pulposus. The geometry of the half discs (Roaf, 1960) was extruded from the mesh to create two independent volume domains (Figure 2: nucleus pulposus and annulus fibrosus). The meshing of the IVD using tetrahedral elements was therefore easier and contact between bone and IVD during the simulations was no longer necessary thanks to the perfect bonding between the meshes. The dimensions of the intervertebral disc are usually taken from measurements (Schroeder et al. 2006, Shirazi-Adl et al. 2010), MRI (Périé et al. 2001, Schmidt et al. 2006) or QCT data (Ayturk et al. 2010, Moramarco et al. 2010, Homminga et al. 2011) assuming the volume of the nucleus and its positioning within the disc (Jones and Wilcox 2008). Thus, a height of 5 mm was used for the two half-intervertebral discs (Amonoo-Kuofi 1991, Inoue et al. 1999) and a volumetric ratio of 42% between nucleus pulposus and annulus fibrosus chosen (Goto et al. 2002, Moramarco et al. 2010). The cranial and caudal mid-surfaces of the discs were chosen flat (Jones and Wilcox 2008).

2.4. Material properties

2.4.1. Bone constitutive model

The elastic and strength properties of each bone element were assigned based on morphology information obtained from the HRpQCT images following the methodology of Pahr and Zysset 2009. This method provides a bone volume fraction map and fabric tensors describing the morphology of the bone. A background grid with a spacing of 3.0 mm was superimposed on the image data. Bone volume fraction and local morphological properties were computed inside a spherical sub-region with a diameter of 7.5 mm diameter centred at each point of the grid. The bone volume fraction in each sub-region was derived from the image data using a calibration curve relating bone volume fraction to apparent bone mineral density (Chevalier et al. 2008). The fabric tensor was calculated using the mean intercept length method (MIL) (Laib et al. 1998) after segmentation of the scan images at a constant threshold (masks). The information was then linearly interpolated between the grid points in order to assign the properties to the elements of the FE mesh.

To model the mechanical behaviour of vertebral bone, a recently proposed visco-plastic damage model by Schwiedrzik and Zysset (2012) was adapted. The rheological model is a damageable elastic spring in series with a plastic pad, which is in parallel with a dashpot element. In the elastic regime, the model shows no strain rate dependence. The plastic strains are accumulating viscously. Damage accumulation is assumed coupled to the plasticity using a damage function reducing all elements of the stiffness tensor. D is limited between 0 (no damage) and 1 (complete failure) accounting for the stiffness reduction of the bone elements due to the formation of micro-cracks. The orthotropic elasticity tensor was assigned to each element based on the morphological information obtained from the images and fabric relationships proposed by Zysset and Curnier (1995) and identified by Rincon and Zysset (2009). The elastic domain is bound by an orthotropic fabric and density based Tsai-Wu criterion that was fitted to the uni and multiaxial strength data of Rincon and Zysset (2009). The viscosity of the plastic accumulation was essentially switched off and the hardening/softening function was identified with experimental force-displacement curves of vertebral sections (Dall'Ara et al. 2010).

2.4.2. Intervertebral disc constitutive model

While linear elastic isotropic models of the disc are available for µFE studies (Homminga et al 2004, Eswaran et al. 2006, Fields et al. 2010), two methods are commonly used to model the anisotropy of the annulus in hFE models: explicit representation of the collagen fibres by bar elements embedded in a matrix (Goto et al. 2002, Rohlmann et al. 2006, Dreischarf et al. 2011) or homogenized hyperelastic constitutive law of the matrix and fibres. This option, developed by Holzapfel and Gasser (2000) to model arteries, was adapted to the annulus fibrosus (Eberlein et al. 2001, Eberlein et al. 2004). Porous models were also developed (Swider et al. 2010, Malandrino et al. 2010, Galbusera et al. 2011) but anisotropic models may be sufficient to represent the instantaneous response of the intervertebral disc (Jones and Wilcox 2008). Therefore, the following free energy functions were derived for the IVD:

$$\psi\text{nucleus} = C_{10}(J_1 - 3) + \frac{1}{\Delta}(J-1)^2$$

$$\psi\text{annulus} = C_{10}(J_1 - 3) + C_{20}(J_1 - 3)^2 + \frac{1}{\Delta}(J-1)^2 + \psi\text{fibres}_4 + \psi\text{fibres}_6$$

$$\psi\text{fibres}_i = \frac{K_1}{2K_2}\{\exp[K_2(J_i - 1)^2] - 1\} \qquad (1)$$

The modified invariants were defined as:

$$J_4 = a_0 C^* a_0$$

$$J_6 = b_0 C^* b_0 \quad (2)$$

with $a_0 = [\cos(\varphi), \sin(\varphi), 0]^t$ and $b_0 = [\cos(\varphi), -\sin(\varphi), 0]^t$) being unitary vectors giving fibres direction and C* is the modified right Green strain tensor:

$$C^* = {}^1\!/_4\, F^{*t} F^* \text{ and } F^* = J^{-1/3} F \quad (3)$$

F is the deformation gradient and J = det(F). This constitutive model was chosen by several authors (Perez del Palomar et al. 2008, Moramarco et al. 2010) and validated against the literature (Brown et al. 1957, Markolf and Morris 1974, Panjabi et al. 1994, Guan et al. 2007). The value of the coefficients C10, C20 (matrix material), Δ (compressibility modulus), K1 and K2 (fibres stiffness) were taken from Moramarco et al. 2010.

An angle $\varphi = \pm 30°$ was chosen relative to a transverse plane and both fibre families were acting only in tension ($J_i < 1$, $\Psi fibres_i = 0$, Peyrault et al. 2009). The fibres were placed circumferentially: thanks to a python script, the local orientation of each annulus elements was defined according to the geometry of the annulus contours. A smooth distribution was achieved by means of a linear interpolation between the orientation at the inner contour around the nucleus and outer contour of the annulus fibrosus (Figure 2).

PMMA was defined as linear isotropic with E = 3000 MPa, ν= 0.3 and prescribed to the nucleus and annulus elementsets without modifying the meshes for the PMMA boundary condition.

2.5. Simulations

The constitutive laws have been implemented as FORTRAN subroutine (UMAT) and non-linear analyses were performed with Abaqus (Abaqus6.9, Simulia, DassaultSystemes, Velizy-Villacoublay, France). The nodes of the caudal surface of the inferior discs were fixed axially and a displacement (PMMA: 3 mm, IVD: 6 mm) was applied on the nodes of the cranial surface of the superior discs at slow constant displacement rate of 5 mm/min (Chevalier et al. 2008). The nodes of both surfaces were free transversely. We computed force-displacement curves, determined the ultimate forces (Ult_{PMMA} and Ult_{IVD}) and damage distribution of the vertebral bodies.

To understand the mechanisms of damage accumulation in bone, the fraction volume damaged (FVD) and weighted mean damage (WMD) were calculated in six element sets. The complete vertebral body, its endplates, cortex and the trabecular bone composed of three sub-

regions: the elements of the trabecular core located underneath the nucleus pulposus (the same elements were picked in case of PMMA boundary condition), the elements besides the cortical wall and the elements of the core (Figure 3).

$$\mathrm{FVD} = \frac{\sum \mathrm{V_i^D}}{\sum \mathrm{V_i}} * 100$$

$$\mathrm{WMD} = \frac{\sum(\mathrm{V_i^D} * \mathrm{D_i})}{\sum \mathrm{V_i}} \quad (4)$$

With V_i being the volume of the i^{th} element of the element set, D_i the damage level of the i^{th} element and V_i^D, the volume of the i^{th} element of the element set if $D_i > 0$. Therefore, $\sum V_i^D$ is the volume of the element set that is damaged. Moreover, WMD describes the extent of damage accumulation within an element set.

2.6. Statistics

Pearson's correlation coefficient (R^2), regression equation, concordance correlation coefficient (ccc, Lin 1989) and standard error was computed for the correlation of ultimate forces between the two loading conditions. Paired two-tailed Student's t-tests were performed for comparisons of volume damaged and weighted mean damaged. Significance level was set to 95% ($p<0.05$).

3. Results

The meshes counted 12000 elements in average. PMMA and IVD simulations lasted 5h and 13h on a four 3 GHz processors PC with 24GB RAM.

3.1. Comparison of force-displacement curves

3.1.1. Verification of the force-displacement curves

Ultimate force was defined as the maximum force reached before softening (Figure 4) and we computed ultimate forces with PMMA (Ult_{PMMA} = 3610 ± 1419 N) and IVD (Ult_{IVD} = 2841 ± 1064 N). Using the same protocol with PMMA, Chevalier et al. (2008) measured experimentally an ultimate force equal to 5339 ± 2138 N and the correlation obtained between our ultimate forces and their experimental measurements is excellent (R^2 = 0.898). By compressing *in vitro* lumbar

vertebrae surrounded by intervertebral discs, Jiang et al. (2010) measured a failure load of 2900 N.

3.1.2. Pre-yield local force maxima

One or several local maxima were seen on force-deflection curves of every IVD simulation before the ultimate force was reached (Figure 4). These peaks were observed in previous *in vitro* tests (Roaf 1960, Henzel et al. 1968, Shirado et al. 1992).

3.1.3. The effect of boundary condition on the yield behaviour

The average Ult_{PMMA} was 22 % higher than Ult_{IVD}. However, excellent correlation was found between Ult_{PMMA} and Ult_{IVD} (R^2= 0.988, ccc = 0.79, std_err = 0.028) (Figure 5). Moreover, in both cases, softening was observed after reaching the ultimate force. However, the decrease in force due to softening was always higher with PMMA than with IVD. The embedded vertebral bodies were also more brittle than the ones with discs and yield occurred earlier. The deformation of the compliant intervertebral discs explains partly these observations but not entirely: embedded specimens appeared also to dissipate more energy than specimens surrounded by discs.

3.2. Comparison of damage localisation

3.2.1. Evolution of damage

The evolution of FVD and WMD during the compression of a vertebral body (Figure 6) shows a faster increase of the volume damaged in trabecular and cortical bonewith PMMA. Moreover, the endplates were more subject to damage when not constrained by the embedding material: the volume of damaged elements and their damage was rising higher and faster.

3.2.2. Damage localization with IVD at the pre-yield local force maxima

One or several local force maxima were observed on the force-deflection curves of the IVD boundary condition. Damage maps of a few increments before (Figure 7 a) and after that peak (Figure 7 b) show that this small but sudden decrease of force seemed to be related to damage initiation in the cancellous bone below the nucleus.

3.2.3. Qualitative observations from damage plots

Coronal views of the damage localisation for a typical specimen (176L4) display the map of damage of the embedded vertebra PMMA and the IVD boundary conditions. They were different, especially in the endplates region. Indeed, at ultimate force (Figure 8 a, c), the highest levels of

damage are seen in the trabecular bone underneath the nuclei, while the embedding seemed to "protect" this area of the bone even for displacements superior to the ultimate displacements (Figure 8 b, d).

3.2.4. Quantitative evaluation of damage

The FVD and WMD were compared between both types of boundary conditions (Figure 9). The volume of cancellous bone damaged was similar for both boundary conditions but the localisation of damage within the trabecular bone itself was studied specifically (Figure 9 a). The fraction of volume damaged in the trabecular core was higher with PMMA (TBCore: FVD_{PMMA} = 66% - FVD_{IVD} = 59%, p = 0.1) but this difference was not significant. The cortical region of the trabecular bone was more likely to damage with PMMA (TBCortex: FVD_{PMMA} = 17% - FVD_{IVD} = 7%, p=0.008) while the trabecular region under the nuclei was more sensible with IVD (TBNucleus: FVD_{PMMA}= 7% / FVD_{IVD} = 19%, p<0.001). Those results were coherent with the FVD of the cortex (FVD_{PMMA}= 65% / FVD_{IVD} = 58%, p = 0.02) and endplates (FVD_{PMMA}= 18% / FVD_{IVD} = 77%, p < 0.001).

However, a quick glance at WMD (Figure 9b) suggests that damage accumulated significantly more in all elementsets ($p_{TBNucleus}$, $p_{TBCortex}$ and $p_{endplate}$< 0.001, p_{TBCore}=0.02) but the cortex when the IVD boundary condition was used. We observed qualitatively that every region of the trabecular bone and the cortical endplates seemed protected when loaded via PMMA. This is also shown by a significantly higher damage level in the complete vertebral body (WMD_{PMMA}= 0.12 – WMD_{IVD} = 0.17, p=0.02).

4. Discussion

Several authors studied the effects of boundary conditions during loading (Homminga et al. 2004, Eswaran et al. 2006, Fields et al. 2010, Homminga et al. 2011) using computationally expensive linear elastic µFE models. They did not attempt to compute the ultimate force, keystone of fracture risk prediction from FE (Crawford et al. 2003, Buckley et al. 2007, Chevalier et al. 2008), nor did they quantify damage in the bone. In this study, we use the state-of-the-art intervertebral disc and bone models to measure the effect of fully degenerated (PMMA) and healthy (IVD) boundary conditions on ultimate force and damage localisation.

A closer look to the force-deflection curves reveals that our simulations are able to capture fine details: local force maxima are seen on every computed force-deflection curves before yield. Interestingly, Roaf (1960), Henzel et al. (1968) and Shirado et al. (1992) observed peaks before

failure of the vertebral body, referring to them as endplates disruptions which is coherent with the sudden increase in damage observed after the peaks in the endplates and trabecular region under the nuclei in i*n vitro* (Jiang et al. 2010), *in vivo* (Ortiz et al. 2011) and *in silico* (Fields et al. 2010) studies. Moreover, this injury is occurring with healthy intervertebral disc as our models of discs.

Ult_{PMMA} is higher than Ult_{IVD}. The force-deflection curves highlight the effects of the boundary condition on ultimate force: the stiffness of the embedding material compared to the relative softness of the healthy intervertebral disc affects the way the endplates distribute stress in the vertebral body and the overall ductility of the vertebral bodies (Nekkanty et al. 2010). Indeed, *in vitro* (Shirado et al. 1992 and Dai 1998) and FE (Homminga et al. 2001, Polikeit et al. 2004) studies reports less risk of fracture for an osteoporotic vertebral body when surrounded by degenerated discs: the trabecular bone acting as an energy absorber carries a higher fraction of the load than the cortical shell when the vertebra is surrounded by healthy discs, while this fraction is lower in case of a stiff degenerated disc (Kurowski and Kubo 1986, Homminga et al. 2001, Adams et al. 2006, Homminga et al. 2011). The underestimation of our FE predictions compared to experimental data is explained by the non-viscous nature of our constitutive law for bone. Although, switching on the viscosity term of the bone material would improve the FE prediction of the ultimate forces measured by Chevalier et al. (2008), this switch would affect equally the FE simulations with PMMA and IVD boundary conditions.

The ability of our models to compute damage localisation provides further insight to our understanding of damage mechanisms. We found that the PMMA embedding keeps the endplates intact whereas damage is easily initiated via intervertebral discs under the nucleus. The stiff embedding material provides rigid boundary conditions that prevent any deformations in the endplates as Fields et al. 2010 showed by suppressing the Poisson effect of the discs. Additional measures show that the endplates and the trabecular bone underneath the nuclei are the weakest regions in osteoporotic vertebral bodies and undergo the highest deformation when loaded with healthy intervertebral discs (Kurowski and Kubo 1986, Eswaran et al. 2007, Fields et al. 2010).

The relative difference Ult_{PMMA}/ Ult_{IVD} is always about 20% and good correlation exists between Ult_{PMMA} and Ult_{IVD} (R^2 = 0.988). This suggests that FE models with embedding material are actually as good as FE models with intervertebral discs to compute vertebral strength of the vertebral bodies knowing the shift between the two predictions (Ult_{IVD}= Ult_{PMMA} * 0.746 + 149.692). Therefore, an explicit modelling of the intervertebral disc does not seem necessary for transversal and longitudinal comparisons of vertebral strength as suggested by Buckley et al. (2006). This high correlation between Ult_{PMMA} and Ult_{IVD} might seem surprising. The stiffness of

the specimen decreases while its overall level of damage increases. However, only a damage localisation band through the entire vertebral body can explain why a specimen reaches ultimate force. This band corresponds approximately to the elements with the lowest BVTV and is independent of the boundary condition, which may explain the high correlation. Therefore, although the growth of damage is depending on the boundary condition, with high areas of damage occurring initially under the endplates with IVD, the damage localisation band at ultimate load presents similarities and the difference between Ult_{PMMA} and Ult_{IVD} becomes almost independent of the specimen tested. The higher damage level under the nuclei explains the non-visibility of "central band of damage" from figure 8 c while visible on Figure 8 a, b, d).

The first limitation to highlight concern the material tested. The number of specimens used is limited (12). However, considering the wide range of age (47-83 y.o.), level (L1-L5), BMD (0.29-1.22 $g.cm^{-2}$) and shape, excellent correlation of ultimate forces and similar damage localisation were computed from our specimens. A second limitation pertains to the damage that does not take in account a pre-existing micro-damage. Finally, we only tested rigid uniaxial compression although sophisticated loading cases were tested (lateral bending, flexion-extension, combined load cases) by Chevalier et al. (2008). However, Chevalier and Zysset (2012) showed that all major stiffnesses correlated well with the axial stiffness. In addition, no experimental tests were performed to validate our spine unit models with the ideal intervertebral discs. Nevertheless, both models of bone and discs had been already validated independently in previous studies (Pahr et al. 2011, Moramarco et al. 2010) and the ultimate forces computed were in agreement with the available literature.

Finally, while embedding of the vertebral endplates is commonly used as a biomechanical testing protocol, our study demonstrated that ultimate force and damage distribution of vertebral bodies were affected significantly by the presence of a soft intervertebral disc using hFE models running 100 times faster than corresponding µFE models even on a standard PC.

5. Acknowledgements

This study was made possible thanks to funding obtained from the European Community, Grant Agreement n° PITN-GA-2009-238690-SPINEFX. The authors would like to thank Yan Chevalier for the HRpQCT data and Dieter Pahr for the support with the in-house software.

6. References

Adams MA, Pollintine P, Tobias JH, Wakley GK, and Dolan P. 2006. Intervertebral Disc Degeneration Can Predispose to Anterior Vertebral Fractures in the Thoracolumbar Spine. J Bone Miner Res. 21(9).

Amonoo-Kuofi HS. 1991. Morphometric changes in the heights and anteroposterior diameters of the lumbar intervertebral discs with age. J Anat. 175:159-168.

Ayturk UM, Garcia JJ and Puttlitz CM. 2010. The micromechanical role of the annulus fibrosus components under physiological loading of the lumbar spine. J Biomech Eng. 132.

Brown T, Hansen RJ, Yorra AJ. 1957. Some mechanical tests on the lumbosacral spine with particular reference to intervertebral disc. J BoneJoint Surg. 39:1135–1164.

Buckley JM, Leang DC, Keaveny TM. 2006. Sensitivity of vertebral compressive strength to endplate loading distribution. J Biomech Eng. 128(5):641–646.

Buckley JM, Cheng L, Loo K, SlyfieldC, and Xu Z. 2007. Quantitative computed tomography-based predictions of vertebral strength in anterior bending. Spine. 329:1019–1027.

Chevalier Y, Charlebois M, Pahr D, Varga P, Heini P, Schneider E, and Zysset P. 2008. A patient-specific finite element methodology to predict damage accumulation in vertebral bodies under axial compression, sagittal flexion and combined loads. Comput Methods Biomech Biomed Eng. 11:477–487.

Chevalier Y and Zysset P. 2012. A patient-specific CT-based finite element methodology to calculate the 6D stiffness matrix of vertebral bodies. Comput Methods Biomech Biomed Eng. 12:77-79.

Crawford RP, Cann CE, and Keaveny TM. 2003. Finite element models predict in vitro vertebral body compressive strength better than quantitative computed tomography. Bone. 334:744–750.

Crawford RP, Rosenberg WS, and Keaveny TM. 2003. Quantitative computed tomography-based finite element models of the human lumbar vertebral body: effect of element size on stiffness, damage, and fracture strength predictions. J Biomech Eng. 1254:434-438.

Dai L. 1998. The relationship between vertebral body deformity and disc degeneration in lumbar

spine of the senile. Eur Spine J. 7:40–44.

Dall'Ara E, Schmidt R, Pahr D, Varga P, Chevalier Y, Patsch J, Kainberger F, Zysset P. 2010. A nonlinear finite element model validation study based on a novel experimental technique for inducing anterior wedge-shape fractures in human vertebral bodies in vitro. J Biomech. 43:2374–2380

Dall'Ara E, Pahr D, Varga P, Kainberger F and Zysset P. 2012. QCT-based finite element models predict human vertebral strength in vitro significantly better than simulated DEXA. Osteoporos Int. 23(2):563-72.

Dolan P and Adams MA. 2001. Recent advances in lumbar spinal mechanics and theirsignificance for modelling. Clinical Biomechanics. 16:S8-S16.

Dreischarf M, Rohlmann A, Bergmann G, Zander T. 2011. Optimised loads for the simulation of axial rotation in the lumbar spine. J Biomech. 44:2323–2327.

Eberlein R, Holzapfel HA and Schulze-Bauer CAJ. 2001. An anisotropic model for annulus tissue and enhanced finite element analyses of intact lumbar disc bodies. Comput Methods Biomech Biomed Eng. 4:209-229.

Eberlein R, Holzapfel G A, Frohlich M. 2004. Multi-segment FEA of the human lumbar spine including the heterogeneity of the annulus fibrosus. Computational Mechanics. 34:147–163.

Eswaran SK, Gupta A, Adams MF, and Keaveny TM. 2006. Cortical and trabecular load sharing in the human vertebral body. J Bone MinerRes. 212:307–314.

Eswaran SK, Gupta A and Keaveny TM 2007. Locations of bone tissue at high risk of initial failure during compressive loading of the human vertebral body. Bone. 41(4):733-739.

Fields AJ, Lee G L and Keaveny TM. 2010. Mechanisms of initial endplate failure in the human vertebral body. J Biomech. 43(16):3126-3131.

Galbusera F, Schmidt H, Neidlinger-Wilke C, Gottschalk A, Wilke HJ. 2011. The mechanical response of the lumbar spine to different combinations of disc degenerative changes investigated using randomized poroelastic finite element models. Eur Spine J. 20:563–571.

Goto K, Tajima N, Chosa E, Totoribe K, Kuroki H, Arizumi Y and Arai T. 2002. Mechanical analysis of the lumbar vertebrae in a three-dimensional finite element method model in which intradiscal pressure in the nucleus pulposus was used to establish the model. J

OrthopSci. 7:243–246.

Graeff C, Chevalier Y, Charlebois M, Varga P, Pahr D, Nickelsen TN, Morlock MM, Glüer CC and Zysset PK. 2009. Improvements in vertebral body strength under teriparatide treatment assessed in vivo by finite element analysis: results from the EUROFORS study. J Bone Miner Res. 24(10):1672-80.

Griffith JF, Genant HK. 2008. Bone mass and architecture determination: state of the art. Best Pract Res ClinEndocrinolMetab. 22:737–764.

Guan Y, Yoganandan N, Moore J, Pintar FA, Zhang J, Maiman DJ, Laud P. 2007. Moment-rotation responses of the lumbosacral spinal column. J Biomech. 40:1975–1980.

Hansson T, Roos B. 1981. The relation between bone mineral content, experimental compression fractures, and disc degeneration in lumbar vertebrae. Spine. 6(2):147-53.

Henzel JH, Mohr GC and von Gierke HE. 1968. Reappraisal of biodynamic implications of human ejections. Aerosp Med. 39(3):231-40.

Holzapfel GA and Gasser TC. 2000. A new constitutive framework for arterial wall mechanics and a comparative study of material models. J Elast. 61: 1–48.

Homminga J, Weinans H, Gowin W, Felsenberg D, Huiskes R. 2001. Osteoporosis changes the amount of vertebral trabecular bone at risk of fracture but not the vertebral load distribution. Spine. 26(14):1555-1561.

Homminga J, and Van-Rietbergen B, Lochmüller E M, Weinans H, Eckstein F and Huiskes R. 2004. The osteoporotic vertebral structure is well adapted to the loads of daily life, but not to infrequent error loads. Bone. 343:510–516.

Homminga J, Aquarius R, Bulsink VE, Jansen CTJ, Verdonschot N. 2011. Can vertebral density changes be explained by intervertebral disc degeneration? Med Eng Phys. 101016/jmedengphy201108003.

Inoue H, Ohmori K, Miyasaka K, Hosoe H. 1999. Radiographic evaluation of the lumbosacral disc height. Skeletal Radiol. 8:638–643.

Jiang G, Luo J, Pollintine P, Dolan P, Adams MA, Eastell R. 2010. Vertebral fractures in the elderly may not always be osteoporotic. Bone. 47:111–116.

Johnell O, Kanis J. 2005. Epidemiology of osteoporotic fractures. Osteoporos Int. 16(Suppl 2):S3–S7.

Jones AC, and Wilcox RK. 2007. Assessment of factors influencing finite element vertebral model predictions. J Biomech Eng. 1296:898–903.

Jones AC and Wilcox RK. 2008. Finite element analysis of the spine: towards a framework of verification, validation and sensitivity analysis. Med Eng Phys. 30:1287–1304.

Keaveny TM, Donley DW, Hoffmann PF, Mitlak BH, Glass EV and Martin JAS. 2007. Effects of teriparatide and alendronate on vertebral strength as assessed by finite element modelling of qct scans in women with osteoporosis. J Bone Miner Res. 221:149–157.

Keller TS, Ziv I, Moeljanto E, Spengler DM. 1993. Interdependence of lumbar disc and subdiscal bone properties: a report of the normal and degenerated spine. J Spinal Disord. 6:106–113.

Kurowski P, Kubo A. 1986. The relationship of degeneration of the intervertebral disc to mechanical loading conditions on lumbar vertebrae. Spine. 11:726-731.

Laib A, Huselmann HJ, Regsegger P. 1998. In vivo high-resolution 3D-QCT of the human forearm. Technol Health Care. 6(5-6):329–337.

Lee Kyu Sung. 2000. The Effect of Disc Degeneration in Osteoporotic Vertebral Fracture. J Korean Soc Spine Surg. 7(4):558-564

Lin L-K, 1989. A concordance correlation coefficient to evaluate reproducibility. Biometrics. 45:255– 268.

Malandrino A, Planell JA, Lacroix D. 2009. Statistical factorial analysis on the poroelastic material properties sensitivity of the lumbar intervertebral disc under compression. Flexion and axial rotation. J Biomech. 42:2780–2788.

Maquer G, Dall'Ara E, Zysset PK. 2012. Removal of the cortical endplates has little effect on ultimate load and damage distribution in QCT-based voxel models of human lumbar vertebrae under axial compression. J Biomech. 45:1733–1738.

McDonnell P, McHugh PE, O'Mahoney D. 2007. Vertebral osteoporosis and trabecular bone quality. Ann Biomed Eng. 35:170–189.

Markolf KL, Morris JM. 1974. The structural components of the vertebral disc: a study of their

contribution to the ability of the disc to withstand compressive force. J Bone Joint Surg. 56:675–687.

Moramarco V, Perez del Palomar A, Pappalettere C, Doblaré M. 2010. An accurate validation of a computational model of a human lumbosacral segment. J Biomech. 43:334–342.

Nekkanty S, Yerramshetty J, Kim D, Zauel R, Johnson E,Cody DD, Yeni YN. 2010. Stiffness of the endplate boundary layer and endplate surface topography are associated with brittleness of human whole vertebral bodies. Bone. 47:783–789.

Ortiz AO and Bordia R. 2011. Injury to the vertebral endplate-disk complex associated with osteoporotic vertebral compression fractures. Am J Neuroradiol. 32:115–20.

Pahr DH and Zysset PK. 2008. From high-resolution CT data to finite element models: development of an integrated modular framework. Comput Methods Biomech Biomed Eng. 12:45-57.

Pahr DH, and Zysset PK. 2009. A comparison of enhanced continuum fe with micro fe models of human vertebral bodies. J Biomech. 424:455-462.

Pahr DH, Dall'Ara E, Varga P and Zysset PK. 2011. HR-pQCT-based homogenised finite element models provide quantitative predictions of experimental vertebral body stiffness and strength with the same accuracy as μFE models. Comput Methods Biomech Biomed Eng. DOI: 10.1080/10255842.2011.556627.

Panjabi MM, Oxland TR, Yamamoto I, Crisco JJ. 1994. Mechanical behavior of the human lumbar and lumbosacral spine as shown by three-dimensional load–displacement curves. J Bone Joint Surg. 76:413-424

Périé D, Sales De Gauzy J, Curnier D, Hobathoc MC. 2001. Intervertebral disc modelling using a MRI method: Migration of the nucleus zone within scoliotic intervertebral discs. Magn Reson Imaging. 19:1245-1248.

Perez del Palomar A, Calvo B, Doblare M. 2008. An accurate finite element model of the cervical spine under quasi-static loading. J Biomech. 41:523-531.

Peyrault F, Renaud C, Labed N, Feng Z. 2009. Modélisation de tissus biologiques en hyperélasticité anisotrope – Étude théorique et approche éléments finis. C R Mécanique. 337:101-106.

Polikeit A, Nolte L, Ferguson S. 2004. Simulated influence of osteoporosis and disc degeneration

on the load transfer in a lumbar functional spinal unit. J Biomech. 37:1061-1069.

Rincon-Kohli L and Zysset P. 2009. Multi-axial mechanical properties of human trabecular bone. J Biomech Model Mechanobiol. 8(3):195–208.

Roaf R. 1960. A study of the mechanism of spinal injuries. J Bone Joint Surg. 42B:810-823.

Rohlmann A, Zander T, Schmidt H, Wilke HJ, Bergmann G. 2006. Analysis of the influence of disc degeneration on the mechanical behaviour of a lumbar motion segment using the finite element method. J Biomech. 39:2484-2490.

Schwiedrzik JJ, Zysset PK. 2012. An anisotropic elastic viscoplastic damage model for bone tissue. Biomech Model Mechanobiol. DOI 101007/s10237-012-0392-9.

Schroeder Y, Wilson W, Huyghe JM, Baaijens FPT. 2006. Osmoviscoelastic finite element model of the intervertebral disc. Eur Spine J. 15(3):S361–71.

Schmidt H, Heuer F, Simon U, Kettler A, Rohlmann A, Claes L. 2006. Application of a new calibration method for a three-dimensional finite element model of a human lumbar annulus fibrosus. ClinBiomech. 21(4):337–44.

Seymour R, Williams LA, Rees JI, Lyons K and Lloyd DCF. 1998. Magnetic Resonance Imaging of Acute Intraosseous Disc Herniation. Clin Radiol. 53:363-368.

Shirado O, Kaneda K, Tadano S, Ishikawa H, McAfee PC and Warden KE. 1992. Influence of disc Degeneration on Mechanisms of Thoracolumbar Burst Fractures. Spine. 17(3):286-92.

Shirazi-Adl A, Taheri M, Urban JPG. 2010. Analysis of cell viability in intervertebral disc: Effect of endplate permeability on cell population. J Biomech. 43:1330-1336.

Swider P, Pedrono A, Ambard D, Accadbled F, Sales de Gauzy J. 2010. Substructuring and poroelastic modelling of the intervertebral disc. J Biomech. 43:1287-1291.

Treece GM, Prager RW, Gee AH. 1999. Regularised marching tetrahedra: improved iso-surface extraction. ComputGraph. 23(4):583-598.

Zysset PK and Curnier A. 1995. An alternative model for anisotropic elasticity based on fabric tensors. Mech Mater. 21(4):243-250.

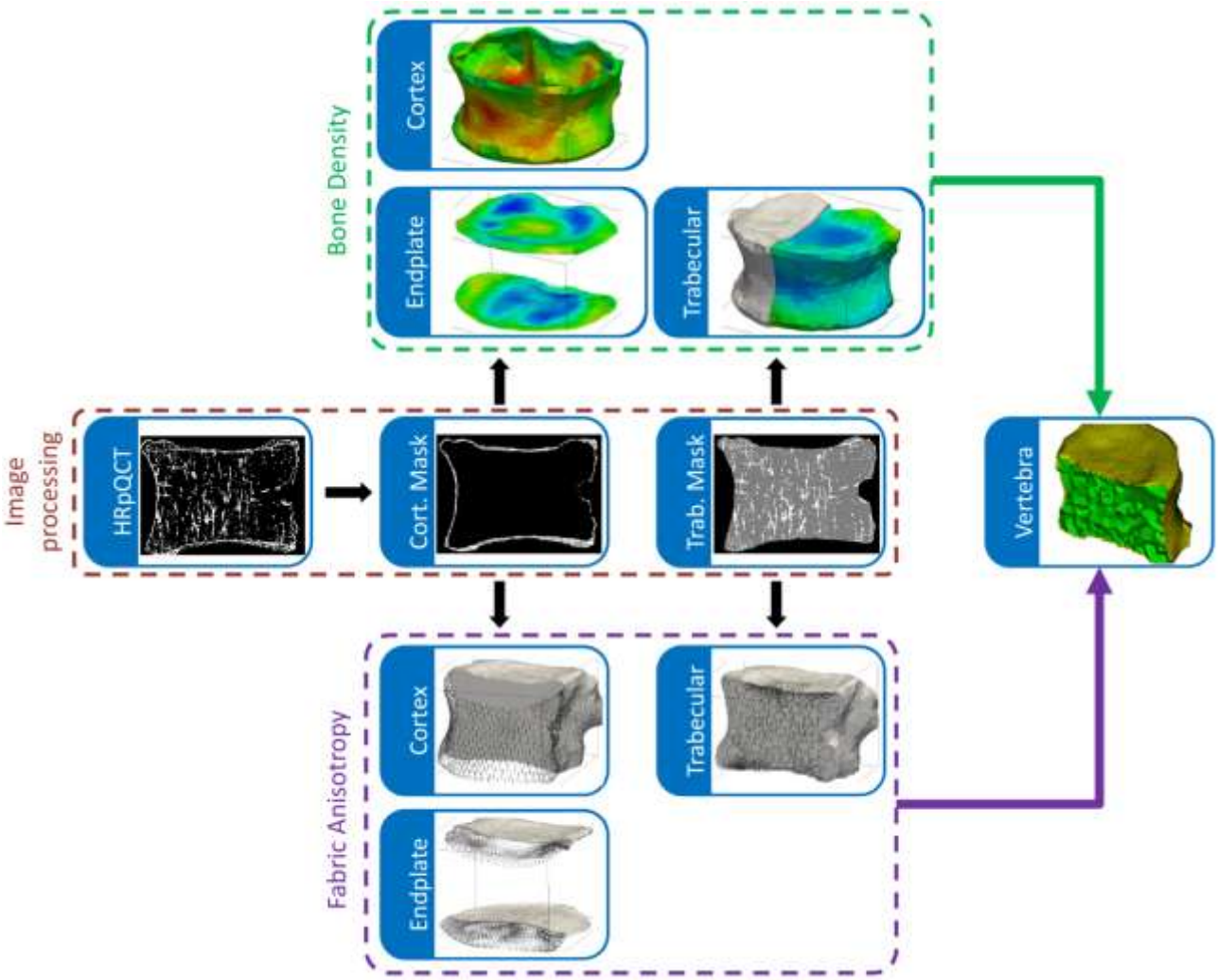

Figure 1. Generation of the homogenized finite element models of the vertebral body.The High Resolution peripheral QCT are segmented, cortical and cancellous bone are separated and three element sets for endplates, cortical and trabecular bone are generated using a published method from the segmented images (Pahr and Zysset 2008). Bone density and fabric are assessed from the CT images for each element (Pahr and Zysset 2009).

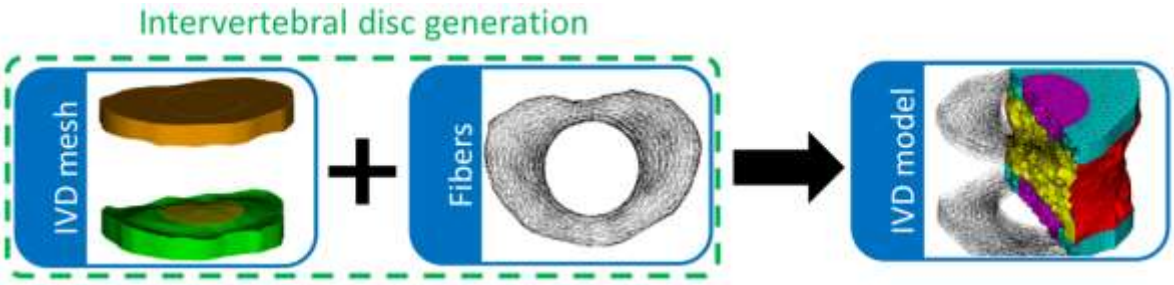

Figure 2. Generation of the intervertebral discs meshes. Two volumes are extruded from the meshes of the cranial and causal cortical endplates of the vertebral body model previously generated. Each volume is separated in two domains to distinguish between nucleus pulposus and annulus fibrosus then meshed. The fibres were oriented circumferentially around the nucleus by changing the local orientation of each annulus element.

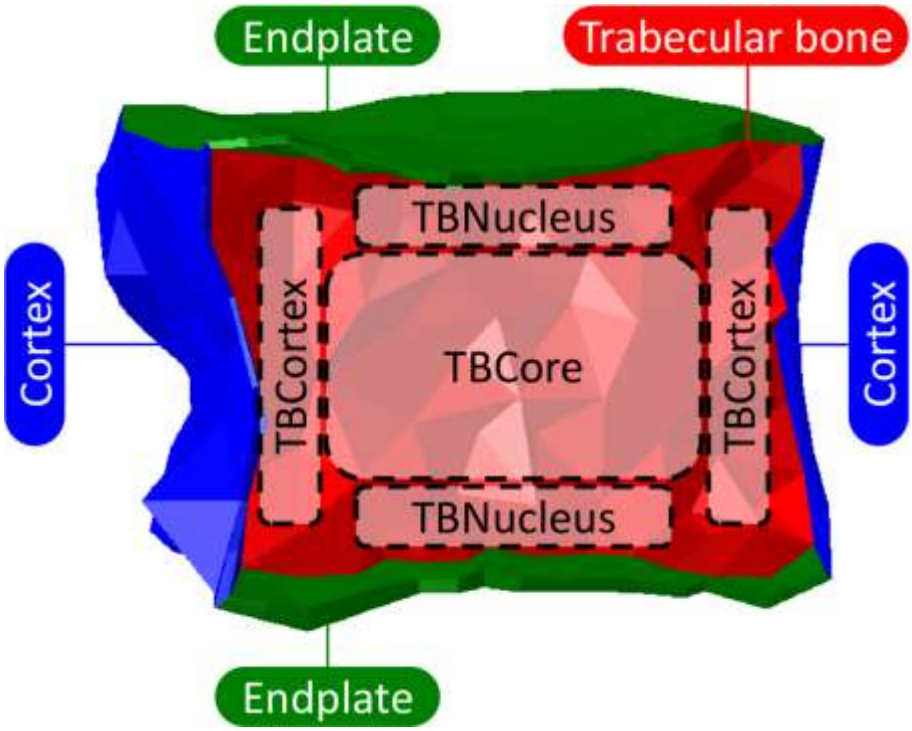

Figure 3. Regions of interest of the vertebral bodies: 1-Subdiscal trabecular elements located underneath the nuclei. 2-Trabecular elements adjacent to cortical wall, 3-Elements of the cancellous core, 4-Cortical endplates, 5-Cortical shell and 6-Full vertebral body.

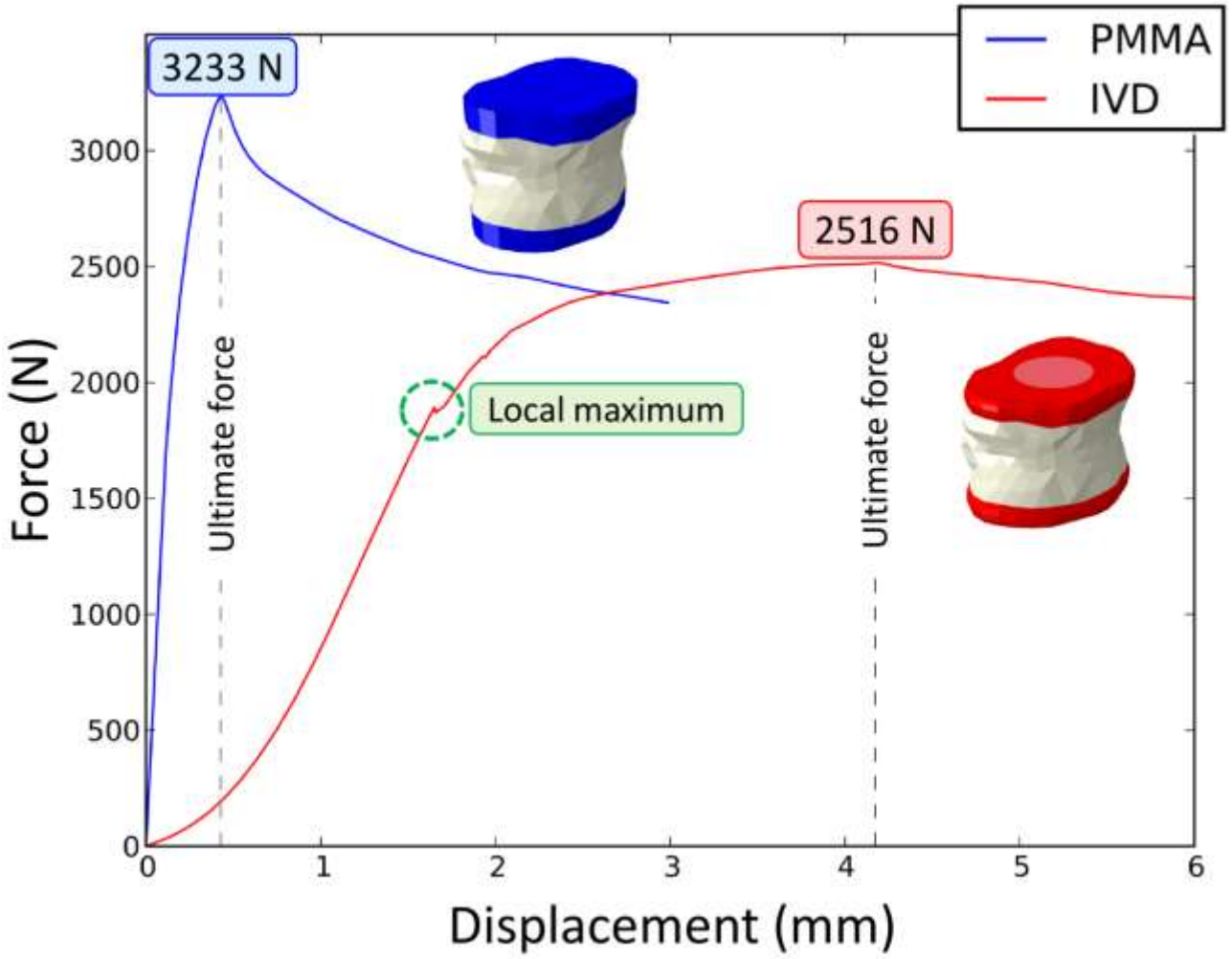

Figure 4. Force-deflection curve computed for the two boundary conditions for a typical vertebral body (176L4). Ultimate forces reported as the maximal force obtained before softening occurs are significantly different ($p<0.0001$).

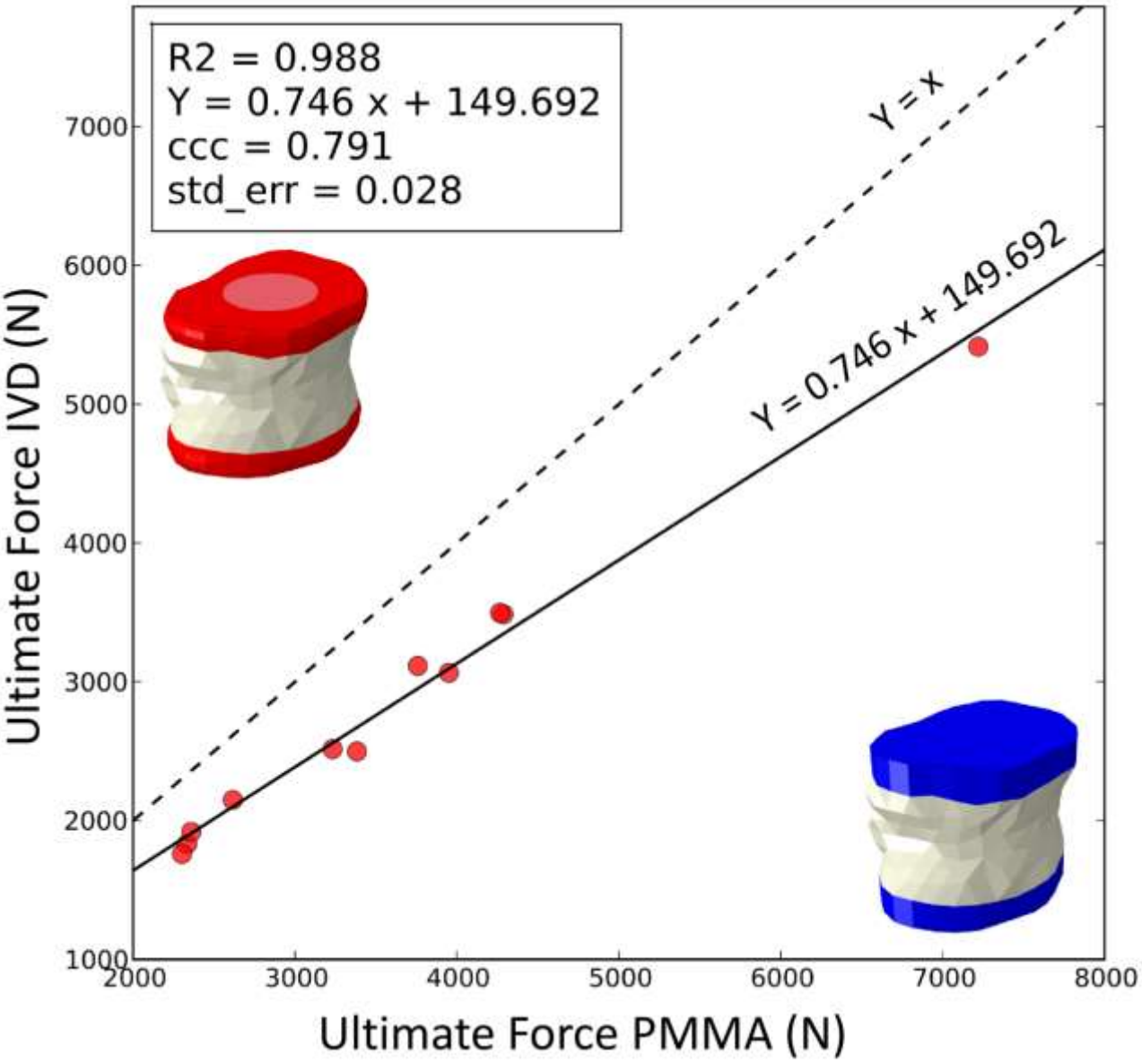

Figure 5. Although the ultimate forces computed IVD and PMMA boundary conditions were significantly different, their correlation was high.

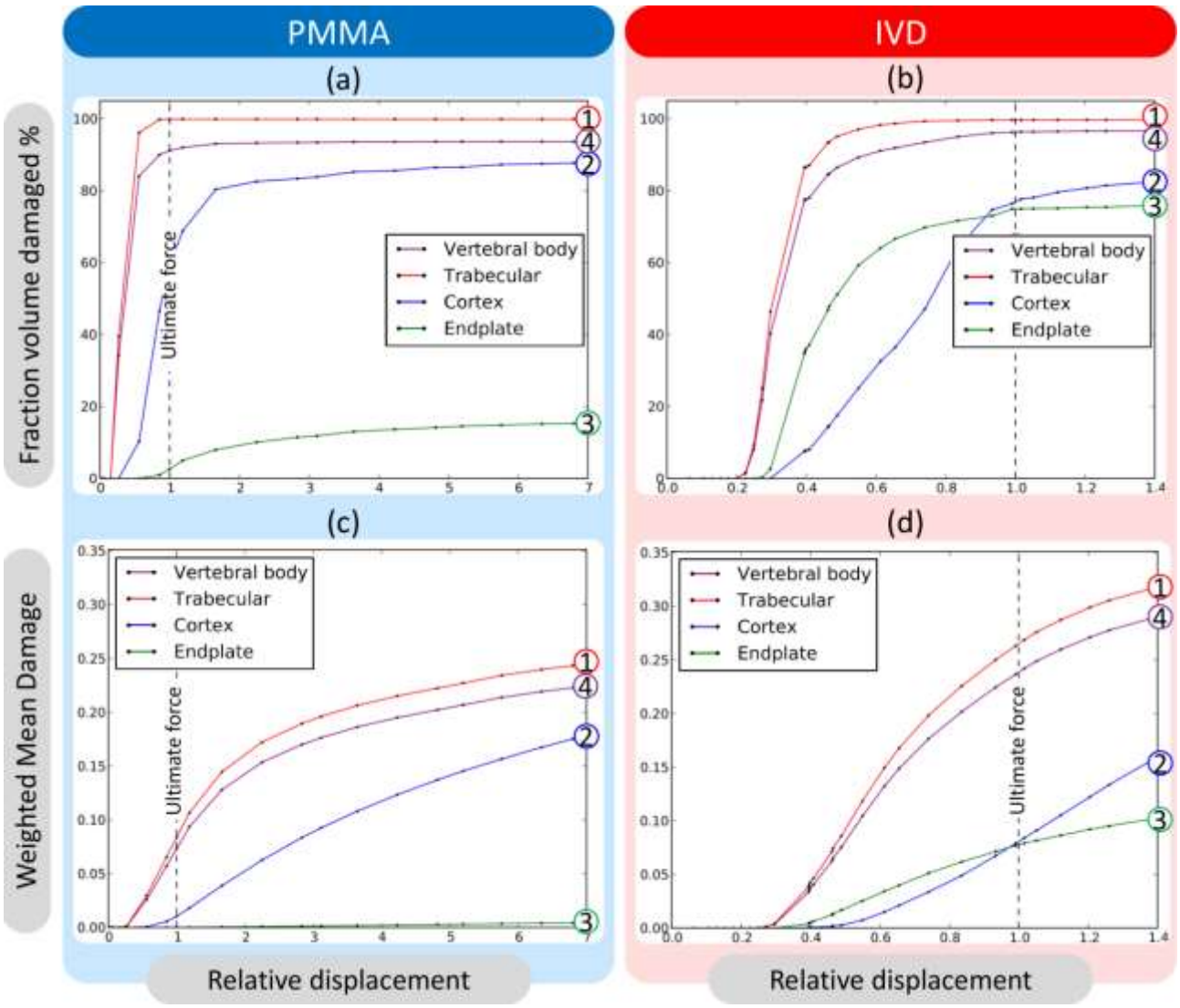

Figure 6. Evolution of the volume damaged (a and b) and of the weighted mean damage (c and d) in the element sets of a typical vertebral body (176L4) plotted against the relative displacement for each boundary condition. The relative displacement is equal to one at the ultimate force. The regions of interest: 1-Trabecular bone. 2-Cortical shell, 3-Cortical endplates and 4-Full vertebral body.

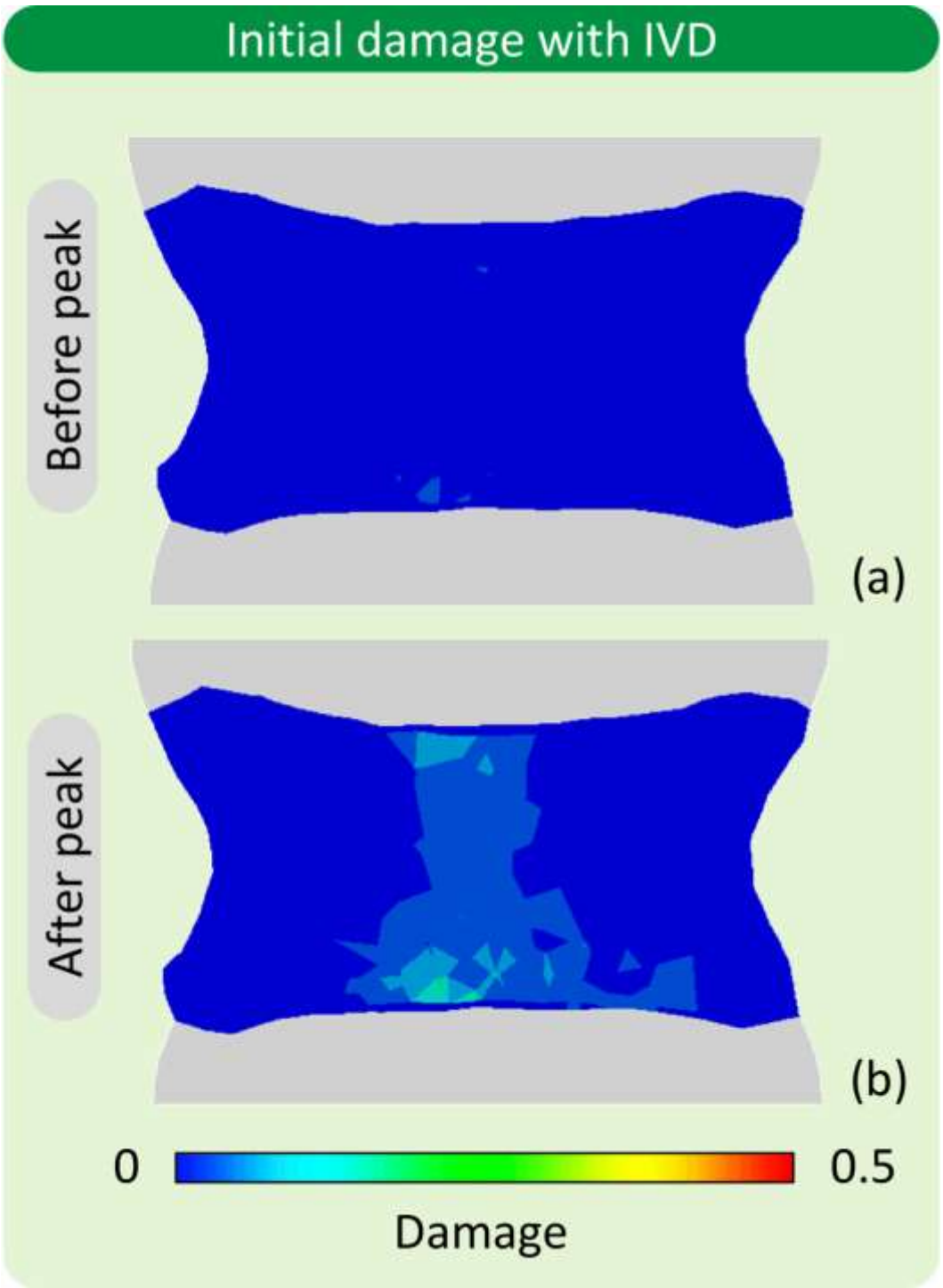

Figure 7. Damage plots before (a) and after (b) the local maximum observed on Figure 4 for the vertebral body 176L4. Damage localisations are displayed on the coronal mid-plane for the IVD boundary condition only.

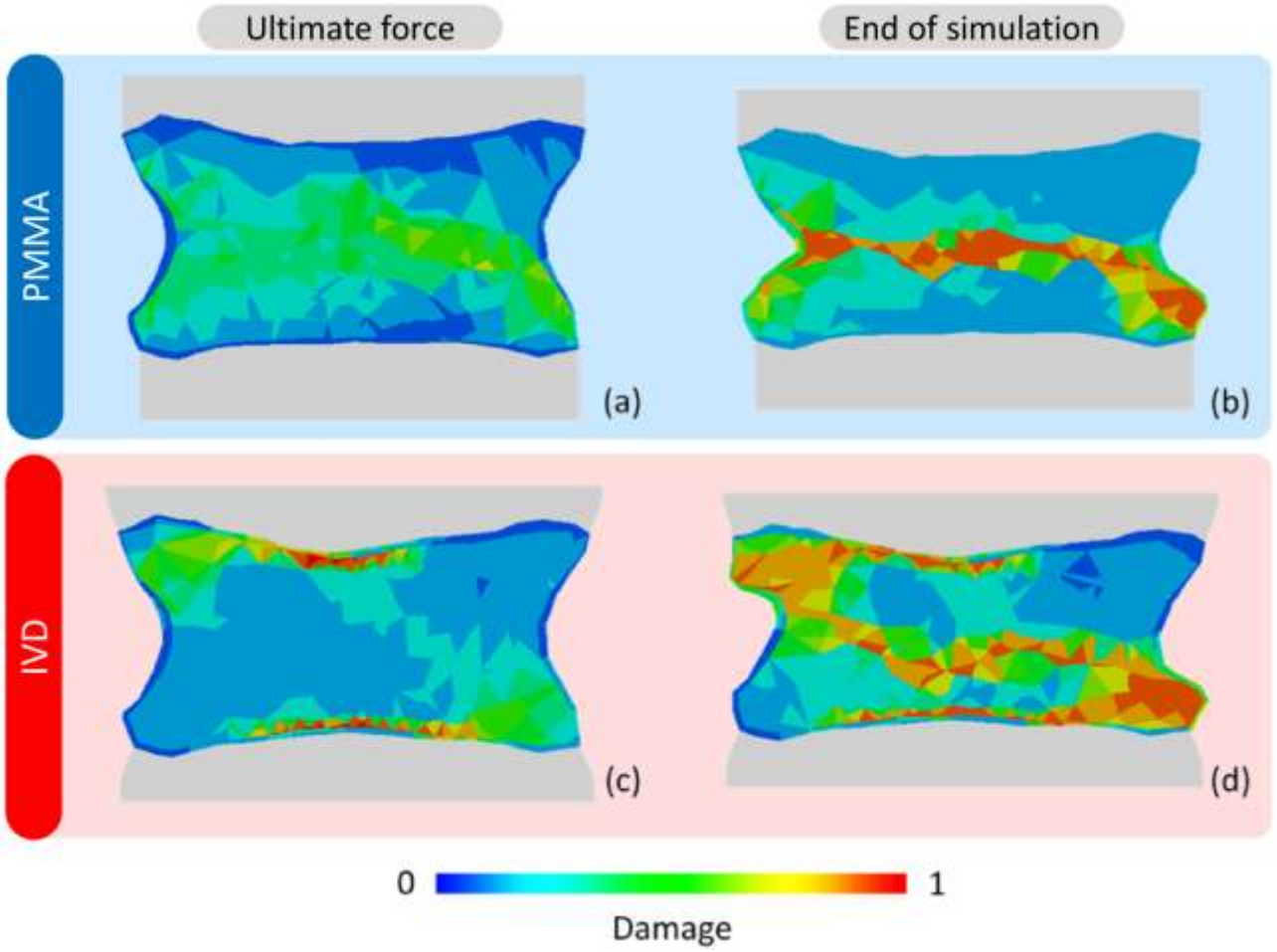

Figure 8. Damage plots during compression of a typical vertebral body (176L4). Damage localisations at ultimate force (a and c) and at the end of the simulation (b and d) are displayed in the coronal mid-plane for each boundary condition.

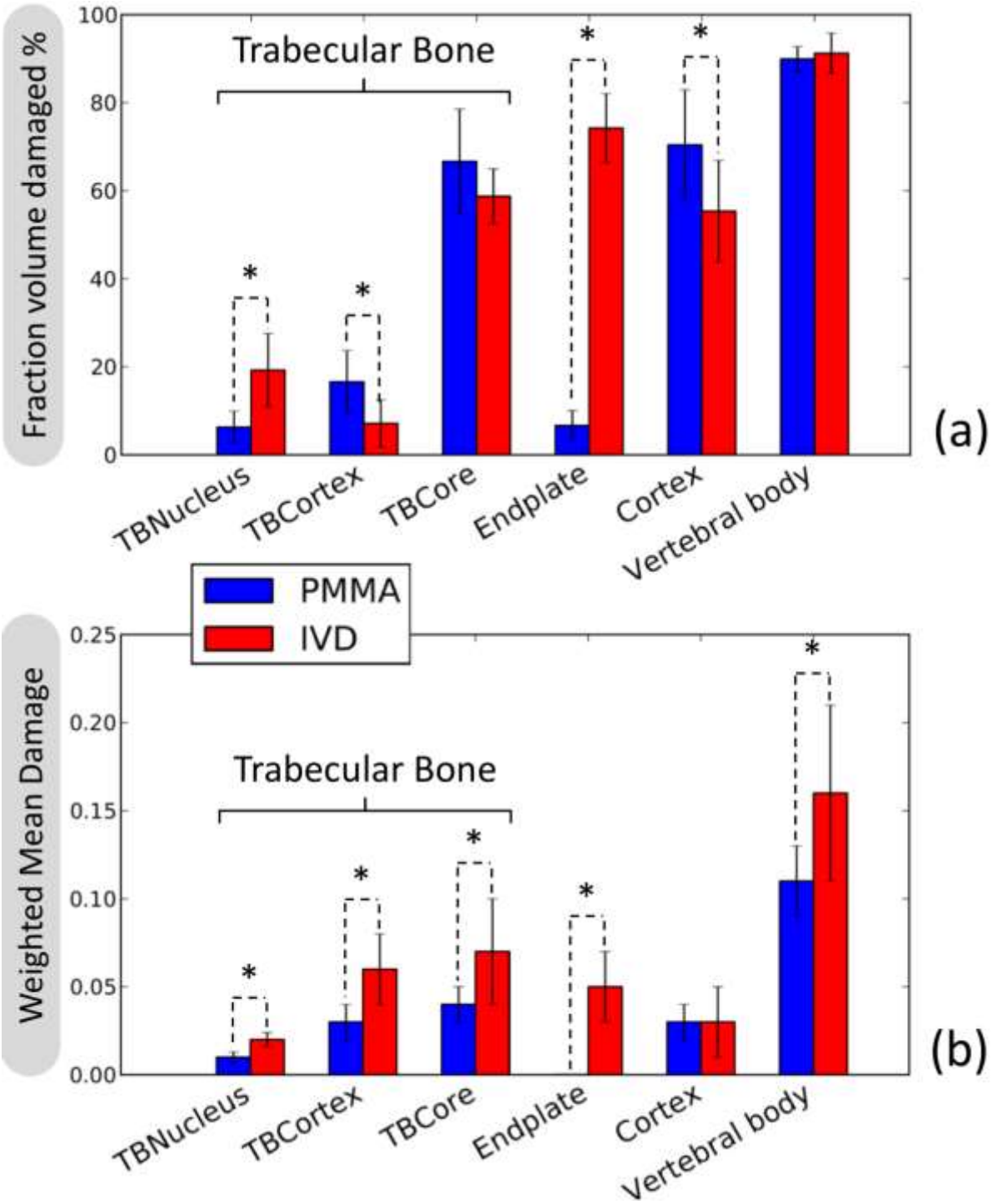

Figure 9. Effect of the boundary conditions on the volume damaged and on the weighted mean damage per regions of interest at ultimate force. The regions of interest: TBNucleus (Subdiscal trabecular elements located underneath the nuclei), TBCortex (Trabecular elements adjacent to cortical wall), TBCore (Elements of the cancellous core), Endplates, Cortex and Vertebral body. Significant differences are marked with *.